

Quantum-corrected thickness-dependent thermal conductivity in amorphous silicon predicted by machine learning molecular dynamics simulations

Yanzhou Wang ^{1,2} Zheyong Fan ^{2,3,*} Ping Qian ^{1,†} Miguel A. Caro ^{4,5} and Tapio Ala-Nissila ^{2,6,‡}

¹Beijing Advanced Innovation Center for Materials Genome Engineering, Department of Physics, University of Science and Technology Beijing, Beijing 100083, China

²Department of Applied Physics, QTF Center of Excellence, Aalto University, FIN-00076 Aalto, Espoo, Finland

³College of Physical Science and Technology, Bohai University, Jinzhou, 121013, China

⁴Department of Electrical Engineering and Automation, Aalto University, FIN-02150 Espoo, Finland

⁵Department of Chemistry and Materials Science, Aalto University, FIN-02150 Espoo, Finland

⁶Interdisciplinary Centre for Mathematical Modelling and Department of Mathematical Sciences, Loughborough University, Loughborough, Leicestershire LE11 3TU, United Kingdom

 (Received 20 June 2022; revised 14 November 2022; accepted 11 January 2023; published 6 February 2023)

Amorphous silicon (a-Si) is an important thermal-management material and also serves as an ideal playground for studying heat transport in strongly disordered materials. Theoretical prediction of the thermal conductivity of a-Si in a wide range of temperatures and sample sizes is still a challenge. Herein we present a systematic investigation of the thermal transport properties of a-Si by employing large-scale molecular dynamics (MD) simulations with an accurate and efficient machine learned neuroevolution potential (NEP) trained against abundant reference data calculated at the quantum-mechanical density-functional-theory level. The high efficiency of NEP allows us to study the effects of finite size and quenching rate in the formation of a-Si in great detail. We find that a simulation cell up to 64 000 atoms (a cubic cell with a linear size of 11 nm) and a quenching rate down to 10^{11} K s⁻¹ are required for almost convergent thermal conductivity. Structural properties, including short- and medium-range order as characterized by the pair-correlation function, angular-distribution function, coordination number, ring statistics, and structure factor are studied to demonstrate the accuracy of NEP and to further evaluate the role of quenching rate. Using both the heterogeneous and homogeneous nonequilibrium MD methods and the related spectral decomposition techniques, we calculate the temperature- and thickness-dependent thermal conductivity values of a-Si and show that they agree well with available experimental results from 10 K to room temperature. Our results also highlight the importance of quantum effects in the calculated thermal conductivity and support the quantum-correction method based on the spectral thermal conductivity.

DOI: [10.1103/PhysRevB.107.054303](https://doi.org/10.1103/PhysRevB.107.054303)

I. INTRODUCTION

Silicon remains as one of the most fundamental semiconductor materials in the microelectronics industry. Amorphous silicon (a-Si) is a disordered semiconductor material with important technological applications, in particular as photoabsorber in solar cells [1,2]. Understanding the thermal properties of a-Si at the atomic level is important in predicting the behavior of this material and how it may affect device performance. Experimental measurements [3–6] have played an important role in characterizing the thermal transport properties of a-Si, but theoretical understanding and reproduction of the experimental results are also important. For pristine crystalline silicon, phonons are the dominant heat carriers and phonon-mediated heat transport has been well understood in terms of anharmonic phonon-phonon scattering within the phonon-gas picture. However, due to the complexity of the

structure and the absence of long-range order [7] in amorphous systems, there are no well-defined phonon bands and the phonon-gas picture is not valid [8]. Most of heat carriers in a-Si are vibrations with short mean-free paths (MFPs) due to the disorder-induced scattering and thus the thermal conductivity in a-Si is about two orders of magnitude smaller than that in crystalline silicon around room temperature [5].

Assuming the dominance of disorder-mediated scattering, a harmonic Hamiltonian model has been proposed by Allen and Feldman [9] and numerical methods based on the Kubo-Greenwood formula have been devised [10], which have led to a classification of lattice vibrations in amorphous materials into propagons, diffusons, and locons corresponding to low, medium, and high-frequency vibrations, respectively [11]. Recently, unified approaches that can account for both anharmonicity and disorder have been developed [12,13], providing a more comprehensive understanding of heat transport from the crystalline to the strongly disordered limit. These methods have found many applications in amorphous or amorphouslike materials, yet they have limitations, such as nonlinear scaling of the computational cost with respect to the simulation cell size and the high cost of including high-order anharmonicity.

*brucenju@gmail.com

†qianping@ustb.edu.cn

‡tapio.ala-nissila@aalto.fi

Molecular dynamics (MD) simulations, on the other hand, have a linear-scaling computational cost with respect to the simulation cell size and contain lattice anharmonicity and phonon scatterings to all orders. MD is the most comprehensive classical atomistic simulation method to study thermal transport and has been the standard approach used for benchmarking other theoretical models or computational methods [12,14,15]. However, reliable application of MD simulations to amorphous materials in general, and to a-Si in particular, is hindered by two main aspects: the scarcity of accurate and efficient interatomic potentials and the classical nature of the MD method.

In this paper, we present solutions to both of the aforementioned obstacles. On the one hand, we develop an accurate yet highly efficient interatomic potential based on machine learning techniques for general silicon systems, applicable to a-Si in particular. There have been some machine learned potentials (MLPs) developed for studying thermal transport in a-Si [16,17], but they are not efficient enough for performing a comprehensive investigation with careful convergence tests. The silicon MLP we develop in this work is based on the neuroevolution potential (NEP) framework [18] which can achieve an unprecedented computational speed of about 10^7 atom step per second using a single Nvidia graphics processing units (GPU) such as Tesla A100. The high accuracy and efficiency of the NEP model allow us to reach a large simulation cell size and long evolution times, generating realistic a-Si structures that closely resemble the experimental samples, which is the prerequisite for obtaining reliable predictions for the thermal transport properties. On the other hand, we apply a proper quantum-statistical correction to the spectral thermal conductivity calculated within the homogeneous nonequilibrium molecular dynamics (HNEMD) formalism [19] and find that this can lead to quantitative agreement with the experimental results [4] in a wide range of temperatures, from 10 K up to the room temperature. With the combination of the efficiency and accuracy of the NEP model and a proper quantum-statistical correction, we achieved insightful results that are difficult to obtain previously.

II. TRAINING A MACHINE LEARNED POTENTIAL FOR a-Si

The NEP model is a neural network (NN) based MLP trained using the separable natural evolution strategy (SNES) [21]. The NN maps the local atom-environment descriptor of a central atom to its site energy and the total energy of an extended system is the sum of the individual site energies of the atoms. The descriptor used in NEP [18] consists of selected radial and angular components similar in spirit to the Behler-Parrinello symmetry functions [22] and the optimized [23] smooth overlap of atomic positions (SOAP) [24].

To train a NEP model applicable to a-Si, we reuse the well-designed training database that has been used to train an accurate Gaussian-approximation potential (GAP) (called GAP18 here) [20]. This training data set was computed at the quantum-mechanical density-functional (DFT) level using the PW91 functional [25] and covers a wide range of silicon structures, including the liquid and a-Si ones in particular. The GAP18 potential has been demonstrated to be well

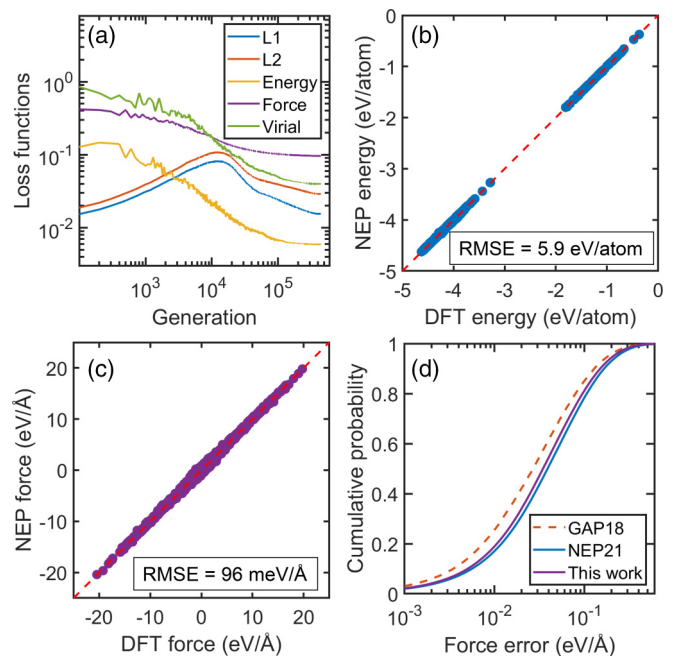


FIG. 1. (a) Evolution of the various terms in the loss function, including those for the \mathcal{L}_1 and \mathcal{L}_2 regularization, the energy root-mean-square error (RMSE) (eV/atom), force RMSE (eV/Å), and virial RMSE (eV/atom) as a function of the training generation. (b) Energy and (c) force calculated from the NEP model as compared to the PW91-density-functional theory (DFT) reference data. The overall converged RMSE of energy and force are presented. (d) Cumulative probability of force error from the NEP model trained in this work as compared to those from the previous NEP21 [18] and GAP18 [20] models.

transferable and is able to simultaneously describe various properties of crystalline and noncrystalline silicon [26]. However, thermal transport usually involves large length and long timescales and GAP18 is not currently efficient enough for this purpose. The NEP model as implemented in the GPUMD package [27,28], on the other hand, can reach a computational speed of about 5×10^6 atom step per second for a-Si by using a single GPU card such as Tesla V100, which is about three orders of magnitude faster than GAP18 using 72 Xeon-Gold 6240 central processing unit (CPU) cores [18].

A NEP model has already been trained previously for benchmarking the NEP framework [18] (we call it NEP21), but with a better understanding on the hyperparameters, we here retrain it by changing the relative weight of virial from 1 to 0.1, keeping all the other hyperparameters as used in Ref. [18] unchanged. Figure 1(a) shows the convergence trend of the root-mean-square error (RMSE) of energy, force, and virial during the training process. We note that both \mathcal{L}_1 and \mathcal{L}_2 regularization are used in our training, which can help to increase the robustness of the potential. Upon convergence, the predicted energy and force from NEP correlate with the reference data very well, as shown in Figs. 1(b) and 1(c). The converged energy and force RMSEs for the training data set are 5.9 meV/atom and 96 meV/Å, respectively. The corresponding RMSEs for the holdout testing data set as used in Ref. [20] are 7.8 meV/atom and 93 meV/Å, respectively. As

TABLE I. Fractions of the different CNs and the average CN ($\overline{\text{CN}}$) from our NEP model for different quenching rates.

α (K s^{-1})	CN = 3	CN = 4	CN = 5	$\overline{\text{CN}}$
10^{11}	0.45%	98.09%	1.46%	4.010
10^{12}	0.61%	96.99%	2.40%	4.018
5×10^{12}	0.79%	95.72%	3.49%	4.027
10^{11} [26]	0.60%	98.36%	1.04%	4.004

can be seen in Fig. 1(d), the NEP model trained in this work is slightly more accurate than NEP21 but is still less accurate than GAP18. This training accuracy is similar to that obtained by using the atomic cluster expansion approach [29]. Despite the relatively lower training accuracy, the NEP trained here exhibits performance on a par with GAP18 in predicting the various structural properties of a-Si, as will be demonstrated below.

III. SAMPLE GENERATION AND STRUCTURAL CHARACTERIZATION

A. Generating a-Si samples

The key ingredient for obtaining reliable results for the physical properties of a-Si is sample preparation. To this end, we use classical MD simulations with a melt-quench-anneal process to prepare the a-Si samples. All the MD simulations are performed using the GPUMD package [27] (version 2.9.1). We take diamond silicon as the initial structure and quickly heat it up to $T_0 = 2000$ K to reach the liquid state and equilibrate it for 0.1 ns. Then, we cool down the system with the target temperature in the thermostat linearly dropping from T_0 to a temperature T (from 10 to 1000 K) with a given quenching rate α (from 5×10^{12} down to 10^{11} K s^{-1}). Finally, we anneal the quenched sample at T for 0.5 ns to obtain a well-equilibrated a-Si structure. We use the isothermal-isobaric ensemble (zero target pressure) realized by the Berendsen thermostat and barostat [31] during the melt-quench-anneal process. We have checked that using the recently proposed Bernetti-Bussi barostat [32] combined with the Bussi-Donadio-Parrinello thermostat [33] does not lead to noticeably different results. In all the MD simulations, we use a time step of 0.5 fs.

Figure 2(a) shows the evolution of the temperature and potential energy in the case of $T = 300$ K and $\alpha = 10^{11}$ K s^{-1} obtained by using a system with $N = 64\,000$ atoms. In this case, the quenching process lasts 17 ns. To appreciate the high computational demands for heat transport applications and the excellent computational efficiency of NEP we note that, to reach the same quenching rate, the system size must be chosen to be $N = 512$ in GAP18 [26] with a time step of 1 fs.

B. Short-range order

After generating the a-Si samples, we first characterize the bond motifs of the short-range order in terms of the pair-correlation function (PCF), the angular-distribution function (ADF), and the coordination number (CN). The results are shown in Fig. 3 and Table I. For the first peak located at about 2.36 Å in the PCF, the height calculated from the NEP model

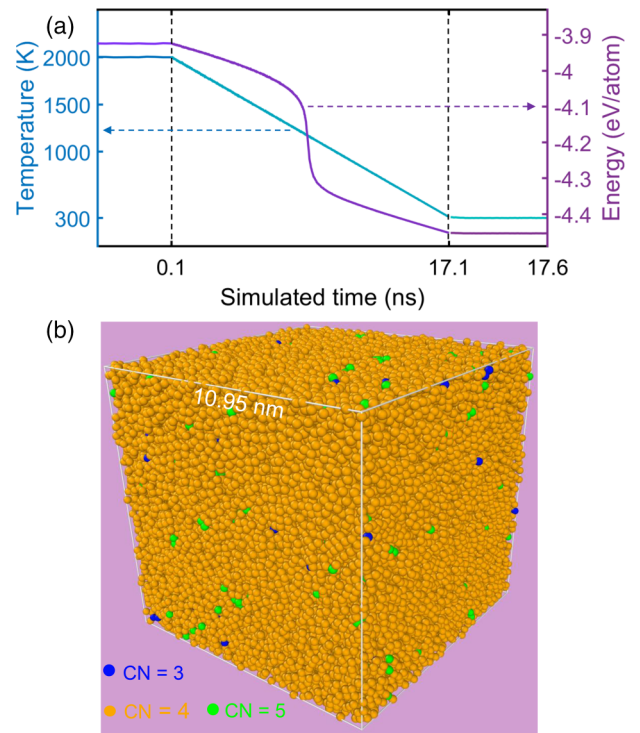


FIG. 2. (a) Temperature and potential energy as a function of simulation time during the melt-quench-anneal process. (b) Snapshot of an a-Si sample after the melt-quench-anneal process, where atoms with different coordination numbers (CN) are rendered in different colors. The OVITO package [30] is used for visualization.

increases with decreasing quenching rate α , getting close to the experimental value [34] when α is reduced to 10^{11} K s^{-1} . The GAP18 model [20] gives a sharper distribution around the first peak. All the theoretical and experimental results agree well beyond the first peak, particularly at the second peak at 3.86 Å.

For the ADF, there are no experimental data, but the NEP and GAP18 models agree well for the same quenching rate $\alpha = 10^{11}$ K s^{-1} . Both show a peak at an angle of 109.5° , indicating the dominance of sp^3 bond motifs in a-Si. Similar to the case of PCF, the peak height in the ADF increases with decreasing quenching rate which indicates that a smaller quenching rate leads to a more locally ordered a-Si structure.

Based on the PCF, we determine the CN of each atom from the neighboring atoms within a cutoff distance of 2.9 Å. The calculated fractions of atoms with different CNs and the average CN are presented in Table I. Most atoms have a CN of 4 and the percentage of these atoms increases from 95.72% to 98.09% as the quenching rate decreases from 5×10^{12} K s^{-1} to 10^{11} K s^{-1} . This trend is in good agreement with that from GAP18 [26]. The results here again indicate that a lower quenching rate leads to a more locally ordered a-Si sample. At the lowest quenching rate here, the averaged CNs from our NEP model and GAP18 are both close to 4. In contrast, the experimentally annealed a-Si samples prepared by ion implantation have an averaged CNs of 3.88 [35]. This can be understood by noting that the experimental a-Si samples are 1.8% less dense than the crystalline precursor that has a CN of 4 due to the appearance of vacancy defects.

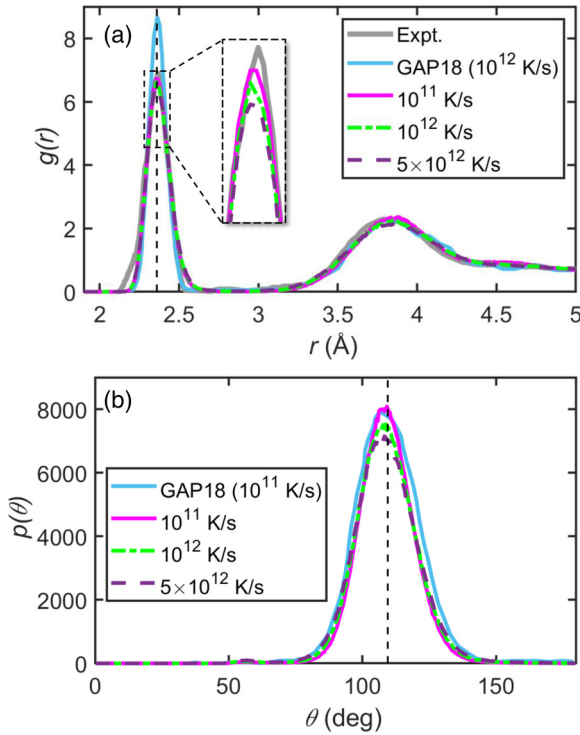


FIG. 3. (a) Pair-correlation function $g(r)$ and (b) angular-distribution function $p(\theta)$ of 64 000-atom a-Si at 300 K generated using different quench rates. The vertical dashed lines in (a) and (b) mark the first peak of $g(r)$ at 2.36 Å and that for $p(\theta)$ at 109.5°, respectively. Experimental measurements [34,35] and theoretical predictions for $g(r)$ [20] and $p(\theta)$ [26] from GAP18 are presented for comparison.

C. Medium-range order

Apart from the short-range order as characterized by the PCF, ADF, and CN, we also characterize the medium-range order. Ring motifs involve the sequential connections of coordination tetrahedra and can be used to characterize near or intermediate medium-range order that is the next length scale following the short-range domain [7]. We compute the ring distribution in Fig. 4(a) using shortest-path algorithm [36]. For crystalline diamond silicon, all atoms are connected to one another in the cyclohexanelike six-membered units with one ring per atom. For a-Si, the most energetically favorable six-membered rings still dominate but seven- and five-membered rings are also energetically viable and exist with a considerable amount as defected motifs in the three-dimensional network of a-Si [26]. With decreasing quench rate, the average number of six-membered rings increases, which indicates an increased near or intermediate medium-range ordering.

The structure factor $S(Q)$, one of the most common experimental structural probes, is typically regarded as a signature of medium-range ordering [7,37,38]. Computationally, $S(Q)$ is typically derived as the Fourier transform of the PCF, i.e., $S(Q) = 1 + 4\pi\rho \int_0^\infty r^2 (\sin Qr/Qr)[g(r) - 1] dr$. For the comparison with diffraction experiments, we also calculate the static $S(Q)$ in Fig. 4(b) using the ISAACS package [39]. The first peak usually gives an indication of intermediate or far medium-range ordering [26,37,38], and we see that it

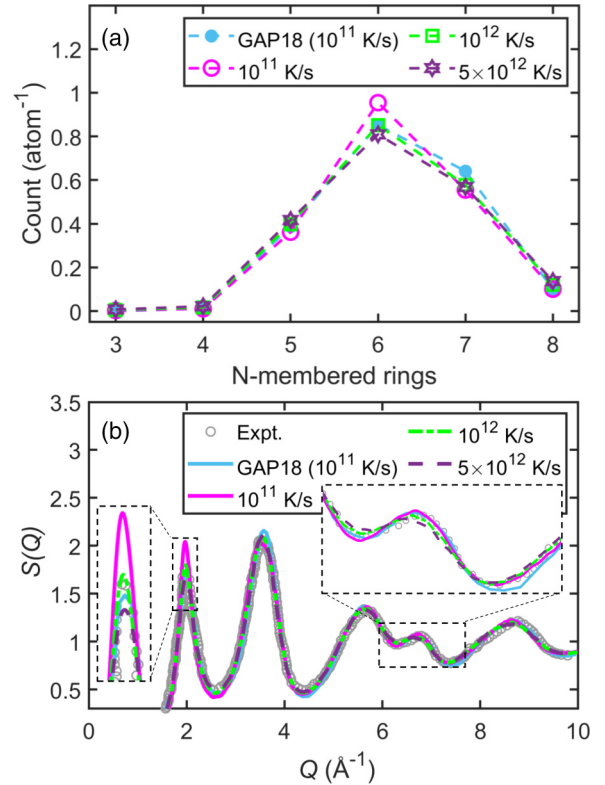


FIG. 4. (a) Number of N -membered rings per atom and (b) structure factor $S(Q)$ as a function of the wave vector Q for a-Si with 64 000 atoms at 300 K. Experimental data [34,35] and prediction from GAP18 [26] are given for comparison.

strengthens [in terms of increased $S(Q)$ value] at about 2 \AA^{-1} with decreasing quenching rate. Specifically for a-Si, there is a direct connection between the first peak in $S(Q)$ and the second peak in the PCF, which corresponds to second-neighbors distances [40]. Also, the shoulder peak at about $Q = 7 \text{ \AA}^{-1}$ features more clearly for lower quenching rate [see inset of Fig. 4(b)]. Indeed, Laaziri *et al.* [35] observed experimentally that annealed a-Si samples exhibit a more featured shoulder peak than as-deposited ones. The quantitative differences between the results from NEP and GAP18 as shown in Fig. 4 are most likely due to the different simulation cell sizes.

IV. HEAT TRANSPORT IN AMORPHOUS SILICON

A. Effects of size and quenching rate on thermal conductivity

After generating and thoroughly characterizing the structures of the a-Si samples, we study their heat transport properties. There are numerous methods for computing thermal conductivity at the atomistic level [41], but MD in particular is efficient for strongly disordered systems. Among the various MD-based methods for thermal conductivity calculations, the HNEMD method has been proven to be the most efficient one [19]. In this method, one applies an external driving force

$$\mathbf{F}_i^{\text{ext}} = \mathbf{F}_e \cdot \mathbf{W}_i, \quad (1)$$

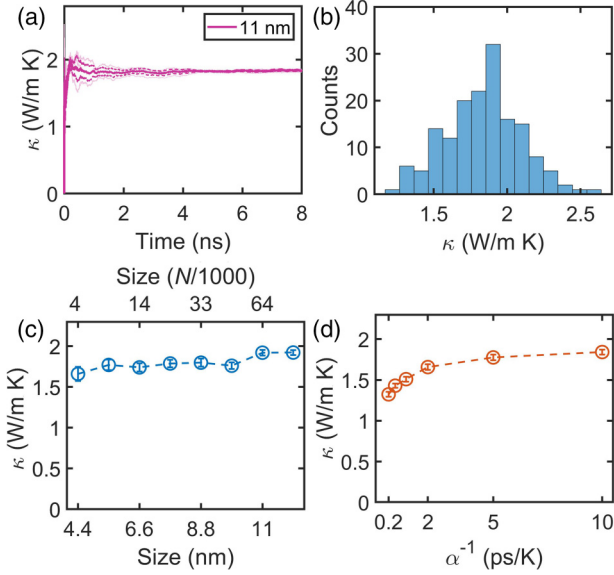


FIG. 5. (a) Cumulative average of the thermal conductivity κ as a function of the HNEMD production time. The thin lines represent results from three independent a-Si samples, and the thick and dashed lines represent the average and error bounds. In this case, the simulation cell size is $N = 64000$ and the quenching rate is $\alpha = 10^{11}$ K s $^{-1}$. (b) Distribution of the block-averaged κ values (each with 0.3 ns) from the HNEMD calculations. (c) κ as a function of the a-Si sample size (indicated as N as well as the linear size of the cubic cell) with $\alpha = 10^{11}$ K s $^{-1}$. (d) κ as a function of inverse quenching rate α^{-1} with $N = 64000$. In all the cases, the temperature is $T = 300$ K.

to create a nonzero heat current. Here \mathbf{F}_e is the driving force parameter with the dimension of inverse length and \mathbf{W}_i is the 3×3 per-atom virial tensor (not necessarily symmetric for many-body potentials) [18,42,43] defined as

$$\mathbf{W}_i = \sum_{j \neq i} \mathbf{r}_{ij} \otimes \frac{\partial U_j}{\partial \mathbf{r}_{ji}}, \quad (2)$$

where \otimes denotes tensor product between two vectors, U_j is the site energy of atom j , and \mathbf{r}_{ij} is defined as $\mathbf{r}_j - \mathbf{r}_i$, \mathbf{r}_i being the position of atom i . In the linear-response regime, the nonequilibrium ensemble average (denoted by $\langle \dots \rangle$) of the heat current \mathbf{J} is proportional to the driving force parameter:

$$\langle \mathbf{J}^\alpha \rangle = TV \sum_{\beta} \kappa^{\alpha\beta} \mathbf{F}_e^\beta, \quad (3)$$

where T is the temperature and V is the volume. Here the instant heat current is calculated based on the definition [18,42,43]

$$\mathbf{J} = \sum_i \mathbf{W}_i \cdot \mathbf{v}_i, \quad (4)$$

where \mathbf{v}_i is the velocity of atom i . The thermal conductivity tensor $\kappa^{\alpha\beta}$ can thus be extracted from Eq. (3). The judicious choices of the magnitude of \mathbf{F}_e for the systems here are presented in Fig. S1 of the Supplemental Material (SM) [44].

Figure 5(a) shows the cumulatively averaged κ versus time in the HNEMD simulations for three independent a-Si

samples with $N = 64000$ atoms obtained with a quenching rate of $\alpha = 10^{11}$ K s $^{-1}$ and a final temperature of $T = 300$ K. We see that κ converges nicely with the simulation time. For temperatures $T < 100$ K, we use six a-Si samples due to the worse ergodicity in MD simulations with decreasing temperature. In all the cases, we treat the trajectories for different samples as a whole and divide them into about 100 equally sized blocks and calculate a proper estimate of the statistical error (measured as the standard error). Figure 5(b) presents the distribution of the block-averaged κ values.

The HNEMD method is physically equivalent to the Green-Kubo method and thus has similar finite-size effects as in the Green-Kubo method [41], which come from two competing effects [45]: a finite cell truncates some long-wavelength vibrations and also ignores some scattering events. In disordered materials, the former should dominate and we expect that κ will increase with increasing simulation cell size. This is indeed the case for our results shown in Fig. 5(c) (see Fig. S2 in the SM [44] for the time convergence of κ for each cell size), where we can see that it requires a system size of $N = 64000$ atoms (or a linear size of 11 nm in a cubic cell) to almost converge κ . This is the size we use for all the subsequent calculations except for those in Sec. IV D, where we explore the effects of finite simulation domain size in more depth.

Similar to the structural properties, κ in a-Si is also sensitive to the quenching rate α , increasing with decreasing α and converging to about 1.82 W m $^{-1}$ K $^{-1}$ at about $\alpha = 2 \times 10^{11}$ K s $^{-1}$ [see Fig. 5(d)] (see Fig. S3 in the SM [44] for the time convergence of κ for each quenching rate). That is, a more ordered structure from a lower quenching rate conducts heat better. Based on the short- and medium-range characterizations, it seems $\alpha = 10^{11}$ K s $^{-1}$ is a safe choice that is also computationally affordable. We thus use this quenching rate in all the subsequent calculations.

It is worth noting that experimentally measured thermal conductivity of a-Si varies from 1.6 to 4 W m $^{-1}$ K $^{-1}$ [3–6,46,47] at room temperature. This large variation is most likely due to the structural differences of the a-Si samples: more ordered samples tend to have higher thermal conductivity according to our results above. For example, Liu *et al.* [46] reported a thermal conductivity of 4 W m $^{-1}$ K $^{-1}$ for a 80- μ m-thick a-Si film deposited by the hot-wire chemical vapor deposition (CVD) method at room temperature, and they confirmed that their a-Si structures are more ordered and possess higher medium-range order than typical ones. Using another flavor of CVD, the vapor-liquid-solid mediated low-pressure CVD, Kwon *et al.* [47] also obtained a thermal conductivity up to 4 W m $^{-1}$ K $^{-1}$ for a 1.7- μ m-thick a-Si film at 300 K. On the other hand, a-Si samples prepared by physical vapor deposition (PVD), such as sputtering deposition [3,5], electron-beam deposition [4], and self-implantation [34,35], tend to be more disordered. Particularly, the a-Si samples by Zink *et al.* are of high purity without crystallinity [4]. Our numerical a-Si sample prepared by the melt-quench-anneal protocol resembles the PVD ones [34,35] as has been shown above. Therefore, we will mainly compare our thermal conductivity results against those by Zink *et al.* [4], which span a large range of temperature (from a few K to a few hundred K).

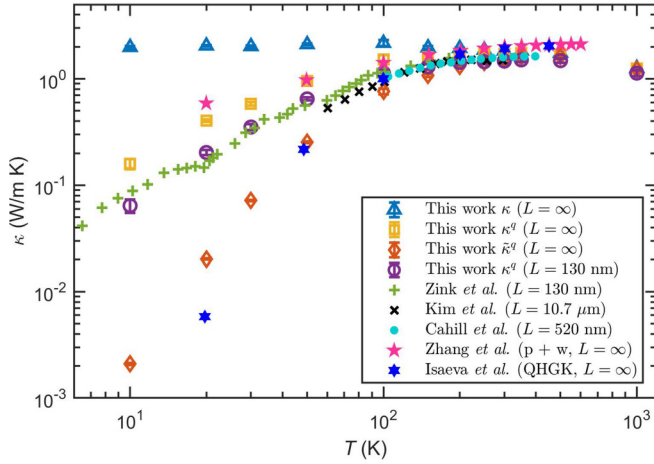


FIG. 6. Thermal conductivity κ as a function of temperature T for a-Si from our calculations as compared to the experimental values by Zink *et al.* [4], Kim *et al.* [6], and Cahill *et al.* [3]. The quasiharmonic Green-Kubo (QHKG) results by Isaeva *et al.* [12] and the theoretical results by Zhang *et al.* [15] based on a particlelike and wavelike (“p + w”) decomposition are also shown for comparison. The sample thickness in the heat transport direction is indicated as L , where $L = \infty$ means the bulk limit.

B. Quantum-statistical correction

After determining the converged N and α , we calculate κ for a-Si at different temperatures and compare the results with experimental ones (see Fig. 6). Figure S4 in the SM [44] presents the time convergence of κ for each temperature. The HNEMD results (triangles) only agree with the experimental ones around and above room temperature, significantly overshooting at low temperatures.

Considering the fact that MD simulations follow classical statistics and the relatively high Debye temperature of silicon (about 487 K) [4], we expect that this overshooting is mostly due to the missing quantum-statistical effects in the MD simulations. To study this in detail, we note that there is a feasible quantum-correction method based on the spectral thermal conductivity in the HNEMD formalism [19]. In this formalism, one can obtain the spectral thermal conductivity $\kappa(\omega, T)$ as a function of the vibrational frequency ω and temperature T with a Fourier transform of the so-called virial-velocity correlation function [19,43], which is a generalization of the spectral heat current approach [48,49] from interface to bulk materials. The virial-velocity correlation function is defined as [19,43]

$$\mathbf{K}(t) = \sum_i \langle \mathbf{W}_i(0) \cdot \mathbf{v}_i(t) \rangle. \quad (5)$$

The summation is over the atoms in a control volume V of interest, and $\langle \dots \rangle$ indicates the average over different time origins. The spectral thermal conductivity is then calculated as

$$\kappa(\omega, T) = \frac{2}{VTF_c} \int_{-\infty}^{\infty} dt e^{i\omega t} K(t). \quad (6)$$

This $\kappa(\omega, T)$ is classical but it can be quantum corrected by multiplying it with a ratio between quantum and classical

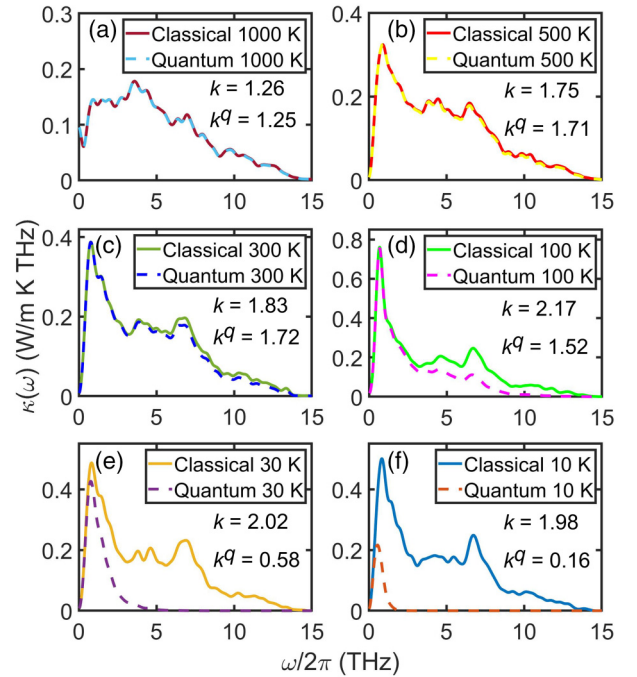


FIG. 7. Classical and quantum-corrected spectral thermal conductivity of a-Si at (a) 1000, (b) 500, (c) 300, (d) 100, (e) 30, and (f) 10 K. Integrated thermal conductivity values are indicated in each panel.

modal heat capacity [50–52]

$$\kappa^q(\omega, T) = \kappa(\omega, T) \frac{x^2 e^x}{(e^x - 1)^2}, \quad (7)$$

where $x = \hbar\omega/k_B T$, \hbar is the reduced Planck constant, and k_B is the Boltzmann constant. The effectiveness of this quantum-correction method for amorphous systems originates from the fact that the population of vibrations has negligible effects on elastic scattering processes. This is in sharp contrast with crystals, where inelastic phonon-phonon scattering dominates and the overpopulated high-frequency phonons in classical MD can reduce the lifetime of the low-frequency phonons and a simple correction of the phonon population usually leads to an underestimated thermal conductivity [53].

Figure 7 shows the classical and quantum-corrected spectral thermal conductivity at different temperatures. Quantum corrections are large at low temperatures and high frequencies, which is consistent with the fact that the populations of the vibrational modes in these conditions are artificially high in classical MD simulations. The total quantum-corrected thermal conductivity $\kappa^q(T)$ is then obtained as an integral of $\kappa^q(\omega, T)$ over the frequency as

$$\kappa^q(T) = \int_0^{\infty} \frac{d\omega}{2\pi} \kappa^q(\omega, T). \quad (8)$$

At room temperature, $\kappa^q(T)/\kappa(T)$ is close to unity at 94%, while it becomes as small as 8.1% at 10 K. The strong quantum-statistical effects make the classical MD results to fail to describe the experimental measurements at low temperatures. After applying the quantum correction, the HNEMD results (squares in Fig. 6) are much closer to the experimental

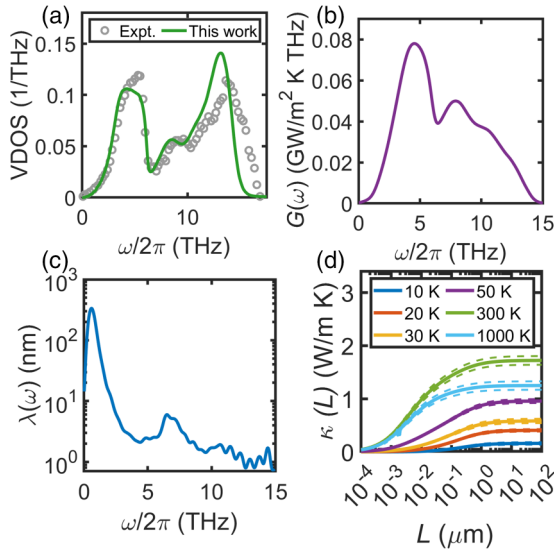


FIG. 8. (a) Vibrational density of states $\rho(\omega)$, (b) classical ballistic spectral thermal conductance $G(\omega)$ at 20 K, and (c) vibrational mean-free path $\lambda(\omega)$ of a-Si as a function of the vibrational frequency $\omega/2\pi$ at 20 K. (d) Quantum-corrected thermal conductivity $\kappa^q(L, T)$ as a function of thickness L of a-Si film in the transport direction. Standard errors are given as dashed lines. Experimental values of $\rho(\omega)$ in (a) are taken from Kamitakahara *et al.* [54].

ones by Zink *et al.* [4], but are still slightly too large at the low-temperature limit. We note that if $\kappa(\omega)$ is not available, one may attempt to make a quantum correction based on the vibrational density of states ($\rho(\omega)$):

$$\tilde{\kappa}^q(T) = \kappa(T) \frac{\int_0^\infty \frac{d\omega}{2\pi} \rho(\omega) \frac{x^2 e^x}{(e^x - 1)^2}}{\int_0^\infty \frac{d\omega}{2\pi} \rho(\omega)}. \quad (9)$$

This is, however, not quantitatively correct because $\rho(\omega)$ does not contain the information of heat transport that is contained in $\kappa(\omega)$ and weights more for the high-frequency part than $\kappa(\omega)$, as can be seen from a comparison between Figs. 8(a) and 7. Therefore, the quantum correction based on $\rho(\omega)$ results in too small a ratio $\tilde{\kappa}^q(T)/\kappa(T)$ as compared

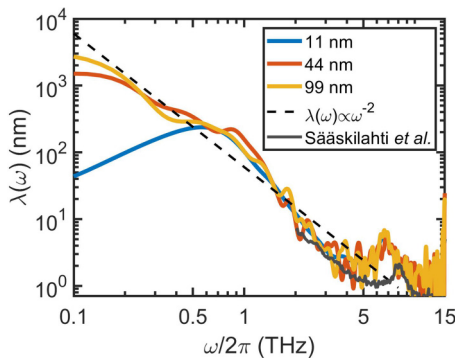


FIG. 9. Vibrational mean-free path $\lambda(\omega)$ with three simulation domain lengths (from 11 to 99 nm) at 300 K. Previous results from Sääskilähti *et al.* [51] are added for comparison. See Figs. S7 and S8 in the SM [44] for details on the HNEMD and spectral decomposition results.

to the correct one $\kappa^q(T)/\kappa(T)$ from the quantum correction based on $\kappa(\omega)$, as can be clearly seen from Fig. 6 (diamond symbols).

C. Length dependence of thermal conductivity

To understand the overestimation of thermal conductivity in the low-temperature limit using the statistical quantum correction (7), we note that the experimental samples are of finite thickness in the transport direction, being $L = 130$ nm [4], while L in our HNEMD simulations should be regarded as infinite. Strong length dependence of κ has been experimentally observed in amorphous silicon thin films [55] or through MFP spectroscopy [56]. To enable a more proper comparison with experiments, we need to compute κ at a finite L . A conventional approach is to perform heterogeneous nonequilibrium molecular dynamics (NEMD) simulations at different L . However, a more computationally efficient and elegant way is to first perform a single NEMD simulation in the ballistic limit (low T and short L) that is equivalent to the atomistic Green's function approach [57], and then employ the same spectral decomposition method as in HNEMD [19] to obtain the spectral thermal conductance $G(\omega)$ [see Fig. 8(b)]:

$$G(\omega) = \frac{2}{V\Delta T} \int_{-\infty}^{\infty} dt e^{i\omega t} K(t). \quad (10)$$

Here ΔT is the temperature difference between the heat source and heat sink in the NEMD setup. After this, one can obtain the spectral MFP as $\lambda(\omega, T) = \kappa(\omega, T)/G(\omega)$ [see Fig. 8(c)], and then obtain the quantum-corrected thermal conductivity at any thickness as [see Fig. 8(d)]

$$\kappa^q(L, T) = \int \frac{d\omega}{2\pi} \frac{\kappa^q(\omega, T)}{1 + \lambda(\omega, T)/L}. \quad (11)$$

Setting $L = 130$ nm as in the experiments [4], our predicted results (circles in Fig. 6) finally agree well with the experimental ones from room temperature down to 10 K.

In Fig. 6, we also present previous theoretical results by Zhang *et al.* [15] and Isaeva *et al.* [12]. The methods in these works have been well benchmarked against their respective MD simulations, but the agreement with experimental data is less satisfactory. These two works have used the Stillinger-Weber [58] and Tersoff [59] empirical potentials, respectively, indicating that these traditional potentials that reproduce pristine Si may not be accurate enough for a-Si. It would thus be interesting to study if combining these methods and our NEP model can improve the results, although this is beyond the scope of this paper.

Finally, to further confirm the reliability of our predictions, we considered possible external stress that can intentionally or accidentally exist in experiments and find that there is no stress dependence of κ^q in a-Si (see Figs. S5 and S6 in the SM [44] for details).

Note that we have considered temperatures up to 1000 K in our calculations, but as far as we know there are no available experimental data at such high temperatures. Based on our results, κ in a-Si at 1000 K is significantly reduced as compared to the room temperature. The validity of this prediction is yet to be confirmed by future experiments. We stress that while the possible contribution to heat conduction by electrons has

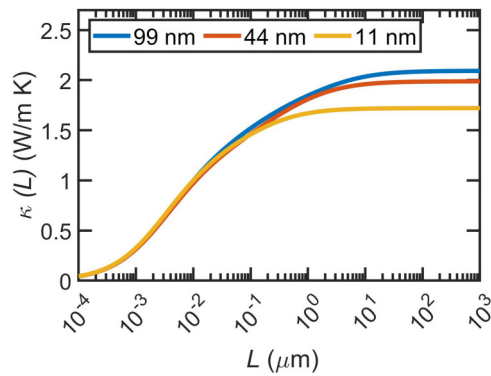


FIG. 10. Quantum-corrected thermal conductivity $\kappa^q(L)$ of a-Si film at 300 K as a function of the film thickness L calculated with three simulation domain lengths (11 to 99 nm).

been ignored in this work, it should not be significant below the melting point of a-Si.

D. Low-frequency limit and finite-size effects

The existence of large vibrational MFPs around 1 THz is a manifestation of the existence of propagons [11]. These propagating phononlike modes contribute a significant portion to the thermal conductivity, which is consistent with experimental measurements [5,55,56] and previous predictions [14,15,60,61]. We note that the MFPs in Fig. 8(c) drop in the low-frequency limit, which is caused by the finite simulation domain length. According to the effective group velocity $v_g \approx 8$ km/s of the propagons [61,62], a domain length of $D = 11$ nm can only support vibrations with frequency down to $v_g/D \approx 0.7$ THz. By considering a domain length up to 99 nm, the lower limit of the frequency that can be probed is pushed down to about 0.08 THz, as can be seen in Fig. 9. We also observe that, in the low-frequency limit, the MFPs scale as $\lambda(\omega) \propto \omega^{-2}$. However, the VDOS scales as $\rho(\omega) \propto \omega^2$ [Fig. 8(a)], leading to a constant contribution to the thermal conductivity. By increasing the domain length from 11 to 99 nm, the total thermal conductivity is only increased by about 15%, but the thickness convergence of the thermal conductivity is extended from about 1 to 10 microns (cf. Fig. 10).

V. SUMMARY AND CONCLUSIONS

In summary, we have studied heat transport in a-Si using extensive MD simulations with an accurate and efficient MLP constructed using the NEP approach. Realistic a-Si samples were first generated using the melt-quench-anneal process. Based on detailed structural analyses and heat transport calculations, we found that both short- and medium-range structural order increase with reduced quenching rate, and the calculated thermal conductivity accordingly increases. A quenching rate of 10^{11} K s⁻¹ is determined to be appropriate to generate realistic a-Si samples and converged thermal conductivity. The thermal conductivity calculated from HNEMD simulations also exhibits notable finite-size effects, requiring a simulation cell with a linear size of 11 nm to reach asymptotic convergence. Based on spectral decomposition techniques, we verified the importance of both quantum statistical effects and a finite sample length commensurate with experiments on the predicted thermal conductivity of a-Si. With a correction to the classical spectral thermal conductivity based on quantum statistics, we obtained good agreement with experiments from 10 K to room temperature using the same sample length. Finally, we also demonstrated that an approximate quantum-correction scheme based on the density of states is inaccurate for a-Si.

The inputs and outputs related to the NEP model training are freely available at the Gitlab repository [63]. The inputs and outputs of all the MD simulations are freely available at Zenodo [64]. The source code of GPUMD is available in [65] and the related documentation can be found in [66].

ACKNOWLEDGMENTS

The authors acknowledge funding from the Academy of Finland, under Projects No. 321713 (M.A.C. and Y. W.), No. 330488 (M.A.C.), No. 312298/QTF Center of Excellence program (T.A.-N., Z.F., and Y.W.), the National Natural Science Foundation of China (NSFC) under Grant No. 11974059 (Z.F.), the National Key Research and Development Program of China under Grant No. 2021YFB3802100 (P.Q. and Y.W.), and the China Scholarship Council under Grant No. CSC202006460064 (Y.W.). The authors also acknowledge computational resources from the Finnish Center for Scientific Computing (CSC) and Aalto University's Science IT project.

[1] M. Stuckelberger, R. Biron, N. Wyrsh, F.-J. Haug, and C. Ballif, Review: Progress in solar cells from hydrogenated amorphous silicon, *Renew. Sustain. Energy Rev.* **76**, 1497 (2017).
 [2] J. Ramanujam, D. M. Bishop, T. K. Todorov, O. Gunawan, J. Rath, R. Nekovei, E. Artagiani, and A. Romeo, Flexible CIGS, CdTe and a-Si:H based thin film solar cells: A review, *Prog. Mater. Sci.* **110**, 100619 (2020).
 [3] D. G. Cahill, M. Katiyar, and J. R. Abelson, Thermal conductivity of a-Si:H thin films, *Phys. Rev. B* **50**, 6077 (1994).
 [4] B. L. Zink, R. Pietri, and F. Hellman, Thermal Conductivity and Specific Heat of Thin-Film Amorphous Silicon, *Phys. Rev. Lett.* **96**, 055902 (2006).

[5] K. T. Regner, D. P. Sellan, Z. Su, C. H. Amon, A. J. H. McGaughey, and J. A. Malen, Broadband phonon mean free path contributions to thermal conductivity measured using frequency domain thermoreflectance, *Nat. Commun.* **4**, 1640 (2013).
 [6] T. Kim, J. Moon, and A. J. Minnich, Origin of micrometer-scale propagation lengths of heat-carrying acoustic excitations in amorphous silicon, *Phys. Rev. Mater.* **5**, 065602 (2021).
 [7] S. R. Elliott, Medium-range structural order in covalent amorphous solids, *Nature (London)* **354**, 445 (1991).
 [8] W. Lv and A. Henry, Examining the validity of the phonon gas model in amorphous materials, *Sci. Rep.* **6**, 37675 (2016).

- [9] P. B. Allen and J. L. Feldman, Thermal conductivity of disordered harmonic solids, *Phys. Rev. B* **48**, 12581 (1993).
- [10] J. L. Feldman, M. D. Kluge, P. B. Allen, and F. Wooten, Thermal conductivity and localization in glasses: Numerical study of a model of amorphous silicon, *Phys. Rev. B* **48**, 12589 (1993).
- [11] P. B. Allen, J. L. Feldman, J. Fabian, and F. Wooten, Diffusons, locons and propagons: Character of atomic vibrations in amorphous Si, *Philos. Mag. B* **79**, 1715 (1999).
- [12] L. Isaeva, G. Barbalinardo, D. Donadio, and S. Baroni, Modeling heat transport in crystals and glasses from a unified lattice-dynamical approach, *Nat. Commun.* **10**, 3853 (2019).
- [13] M. Simoncelli, N. Marzari, and F. Mauri, Unified theory of thermal transport in crystals and glasses, *Nat. Phys.* **15**, 809 (2019).
- [14] Y. Zhou, Assessing the quantum effect in classical thermal conductivity of amorphous silicon, *J. Appl. Phys.* **129**, 235104 (2021).
- [15] Z. Zhang, Y. Guo, M. Bescond, J. Chen, M. Nomura, and S. Volz, How coherence is governing diffuson heat transfer in amorphous solids, *npj Comput. Mater.* **8**, 96 (2022).
- [16] X. Qian, S. Peng, X. Li, Y. Wei, and R. Yang, Thermal conductivity modeling using machine learning potentials: Application to crystalline and amorphous silicon, *Mater. Today Phys.* **10**, 100140 (2019).
- [17] R. Li, E. Lee, and T. Luo, A unified deep neural network potential capable of predicting thermal conductivity of silicon in different phases, *Mater. Today Phys.* **12**, 100181 (2020).
- [18] Z. Fan, Z. Zeng, C. Zhang, Y. Wang, K. Song, H. Dong, Y. Chen, and T. Ala-Nissila, Neuroevolution machine learning potentials: Combining high accuracy and low cost in atomistic simulations and application to heat transport, *Phys. Rev. B* **104**, 104309 (2021).
- [19] Z. Fan, H. Dong, A. Harju, and T. Ala-Nissila, Homogeneous nonequilibrium molecular dynamics method for heat transport and spectral decomposition with many-body potentials, *Phys. Rev. B* **99**, 064308 (2019).
- [20] A. P. Bartók, J. Kermode, N. Bernstein, and G. Csányi, Machine Learning a General-Purpose Interatomic Potential for Silicon, *Phys. Rev. X* **8**, 041048 (2018).
- [21] T. Schaul, T. Glasmachers, and J. Schmidhuber, High Dimensions and Heavy Tails for Natural Evolution Strategies, *Proceedings of the 13th Annual Conference on Genetic and Evolutionary Computation*, GECCO '11 (Association for Computing Machinery, New York, 2011), pp. 845–852.
- [22] J. Behler, Atom-centered symmetry functions for constructing high-dimensional neural network potentials, *J. Chem. Phys.* **134**, 074106 (2011).
- [23] M. A. Caro, Optimizing many-body atomic descriptors for enhanced computational performance of machine learning based interatomic potentials, *Phys. Rev. B* **100**, 024112 (2019).
- [24] A. P. Bartók, R. Kondor, and G. Csányi, On representing chemical environments, *Phys. Rev. B* **87**, 184115 (2013).
- [25] J. P. Perdew, J. A. Chevary, S. H. Vosko, K. A. Jackson, M. R. Pederson, D. J. Singh, and C. Fiolhais, Atoms, molecules, solids, and surfaces: Applications of the generalized gradient approximation for exchange and correlation, *Phys. Rev. B* **46**, 6671 (1992).
- [26] V. L. Deringer, N. Bernstein, A. P. Bartók, M. J. Cliffe, R. N. Kerber, L. E. Marbella, C. P. Grey, S. R. Elliott, and G. Csányi, Realistic atomistic structure of amorphous silicon from machine-learning-driven molecular dynamics, *J. Phys. Chem. Lett.* **9**, 2879 (2018).
- [27] Z. Fan, W. Chen, V. Vierimaa, and A. Harju, Efficient molecular dynamics simulations with many-body potentials on graphics processing units, *Comput. Phys. Commun.* **218**, 10 (2017).
- [28] Z. Fan, Y. Wang, P. Ying, K. Song, J. Wang, Y. Wang, Z. Zeng, K. Xu, E. Lindgren, J. M. Rahm, A. J. Gabourie, J. Liu, H. Dong, J. Wu, Y. Chen, Z. Zhong, J. Sun, P. Erhart, Y. Su, and T. Ala-Nissila, GPUMD: A package for constructing accurate machine-learned potentials and performing highly efficient atomistic simulations, *J. Chem. Phys.* **157**, 114801 (2022).
- [29] G. Dusson, M. Bachmayr, G. Csányi, R. Drautz, S. Etter, C. van der Oord, and C. Ortner, Atomic cluster expansion: Completeness, efficiency and stability, *J. Comput. Phys.* **454**, 110946 (2022).
- [30] A. Stukowski, Visualization and analysis of atomistic simulation data with OVITO—the Open Visualization Tool, *Modell. Simul. Mater. Sci. Eng.* **18**, 015012 (2010).
- [31] H. J. C. Berendsen, J. P. M. Postma, W. F. Van Gunsteren, A. DiNola, and J. R. Haak, Molecular dynamics with coupling to an external bath, *J. Chem. Phys.* **81**, 3684 (1984).
- [32] M. Bernetti and G. Bussi, Pressure control using stochastic cell rescaling, *J. Chem. Phys.* **153**, 114107 (2020).
- [33] G. Bussi, D. Donadio, and M. Parrinello, Canonical sampling through velocity rescaling, *J. Chem. Phys.* **126**, 014101 (2007).
- [34] K. Laaziri, S. Kycia, S. Roorda, M. Chicoine, J. L. Robertson, J. Wang, and S. C. Moss, High Resolution Radial Distribution Function of Pure Amorphous Silicon, *Phys. Rev. Lett.* **82**, 3460 (1999).
- [35] K. Laaziri, S. Kycia, S. Roorda, M. Chicoine, J. L. Robertson, J. Wang, and S. C. Moss, High-energy x-ray diffraction study of pure amorphous silicon, *Phys. Rev. B* **60**, 13520 (1999).
- [36] D. S. Franzblau, Computation of ring statistics for network models of solids, *Phys. Rev. B* **44**, 4925 (1991).
- [37] M. Hejna, P. J. Steinhardt, and S. Torquato, Nearly hyperuniform network models of amorphous silicon, *Phys. Rev. B* **87**, 245204 (2013).
- [38] R. Xie, G. G. Long, S. J. Weigand, S. C. Moss, T. Carvalho, S. Roorda, M. Hejna, S. Torquato, and P. J. Steinhardt, Hyperuniformity in amorphous silicon based on the measurement of the infinite-wavelength limit of the structure factor, *Proc. Natl. Acad. Sci. USA* **110**, 13250 (2013).
- [39] S. Le Roux and V. Petkov, ISAACS—interactive structure analysis of amorphous and crystalline systems, *J. Appl. Crystallogr.* **43**, 181 (2010).
- [40] D. Dahal, H. Warren, and P. Biswas, On the origin and structure of the first sharp diffraction peak of amorphous silicon, *Phys. Status Solidi B* **258**, 2000447 (2021).
- [41] X. Gu, Z. Fan, and H. Bao, Thermal conductivity prediction by atomistic simulation methods: Recent advances and detailed comparison, *J. Appl. Phys.* **130**, 210902 (2021).
- [42] Z. Fan, Luiz Felipe C. Pereira, H.-Q. Wang, J.-C. Zheng, D. Donadio, and A. Harju, Force and heat current formulas for many-body potentials in molecular dynamics simulations with applications to thermal conductivity calculations, *Phys. Rev. B* **92**, 094301 (2015).
- [43] A. J. Gabourie, Z. Fan, T. Ala-Nissila, and E. Pop, Spectral decomposition of thermal conductivity: Comparing velocity decomposition methods in homogeneous molecular dynamics simulations, *Phys. Rev. B* **103**, 205421 (2021).

- [44] See Supplemental Material at <http://link.aps.org/supplemental/10.1103/PhysRevB.107.054303> for detailed cumulative average of the thermal conductivities and spectral thermal conductivities of amorphous silicon.
- [45] A. J. C. Ladd, B. Moran, and W. G. Hoover, Lattice thermal conductivity: A comparison of molecular dynamics and anharmonic lattice dynamics, *Phys. Rev. B* **34**, 5058 (1986).
- [46] X. Liu, J. L. Feldman, D. G. Cahill, R. S. Crandall, N. Bernstein, D. M. Photiadis, M. J. Mehl, and D. A. Papaconstantopoulos, High Thermal Conductivity of a Hydrogenated Amorphous Silicon Film, *Phys. Rev. Lett.* **102**, 035901 (2009).
- [47] S. Kwon, J. Zheng, M. C. Wingert, S. Cui, and R. Chen, Unusually high and anisotropic thermal conductivity in amorphous silicon nanostructures, *ACS Nano* **11**, 2470 (2017).
- [48] K. Sääskilähti, J. Oksanen, J. Tulkki, and S. Volz, Role of anharmonic phonon scattering in the spectrally decomposed thermal conductance at planar interfaces, *Phys. Rev. B* **90**, 134312 (2014).
- [49] K. Sääskilähti, J. Oksanen, S. Volz, and J. Tulkki, Frequency-dependent phonon mean free path in carbon nanotubes from nonequilibrium molecular dynamics, *Phys. Rev. B* **91**, 115426 (2015).
- [50] W. Lv and A. Henry, Direct calculation of modal contributions to thermal conductivity via Green–Kubo modal analysis, *New J. Phys.* **18**, 013028 (2016).
- [51] K. Sääskilähti, J. Oksanen, J. Tulkki, A. J. H. McGaughey, and S. Volz, Vibrational mean free paths and thermal conductivity of amorphous silicon from non-equilibrium molecular dynamics simulations, *AIP Adv.* **6**, 121904 (2016).
- [52] Z. Fan, P. Hirvonen, L. F. C. Pereira, M. M. Ervasti, K. R. Elder, D. Donadio, A. Harju, and T. Ala-Nissila, Bimodal grain-size scaling of thermal transport in polycrystalline graphene from large-scale molecular dynamics simulations, *Nano Lett.* **17**, 5919 (2017).
- [53] J. E. Turney, A. J. H. McGaughey, and C. H. Amon, Assessing the applicability of quantum corrections to classical thermal conductivity predictions, *Phys. Rev. B* **79**, 224305 (2009).
- [54] W. A. Kamitakahara, C. M. Soukoulis, H. R. Shanks, U. Buchenau, and G. S. Grest, Vibrational spectrum of amorphous silicon: Experiment and computer simulation, *Phys. Rev. B* **36**, 6539 (1987).
- [55] J. L. Braun, C. H. Baker, A. Giri, M. Elahi, K. Artyushkova, T. E. Beechem, P. M. Norris, Z. C. Leseman, J. T. Gaskins, and P. E. Hopkins, Size effects on the thermal conductivity of amorphous silicon thin films, *Phys. Rev. B* **93**, 140201(R) (2016).
- [56] Y. Pan, J. Zhou, and G. Chen, Quantifying thermal transport in amorphous silicon using mean free path spectroscopy, *Phys. Rev. B* **101**, 144203 (2020).
- [57] Z. Li, S. Xiong, C. Sievers, Y. Hu, Z. Fan, N. Wei, H. Bao, S. Chen, D. Donadio, and T. Ala-Nissila, Influence of thermostatting on nonequilibrium molecular dynamics simulations of heat conduction in solids, *J. Chem. Phys.* **151**, 234105 (2019).
- [58] F. H. Stillinger and T. A. Weber, Computer simulation of local order in condensed phases of silicon, *Phys. Rev. B* **31**, 5262 (1985).
- [59] J. Tersoff, Modeling solid-state chemistry: Interatomic potentials for multicomponent systems, *Phys. Rev. B* **39**, 5566 (1989).
- [60] J. M. Larkin and A. J. H. McGaughey, Thermal conductivity accumulation in amorphous silica and amorphous silicon, *Phys. Rev. B* **89**, 144303 (2014).
- [61] J. Moon, B. Latour, and A. J. Minnich, Propagating elastic vibrations dominate thermal conduction in amorphous silicon, *Phys. Rev. B* **97**, 024201 (2018).
- [62] J. Moon, R. P. Hermann, M. E. Manley, A. Alatas, A. H. Said, and A. J. Minnich, Thermal acoustic excitations with atomic-scale wavelengths in amorphous silicon, *Phys. Rev. Mater.* **3**, 065601 (2019).
- [63] <https://gitlab.com/brucefan1983/nep-data>.
- [64] Y. Wang, Z. Fan, P. Qian, M. A. Caro, and T. Ala-Nissila, Data for “Quantum-corrected thickness-dependent thermal conductivity in amorphous silicon predicted by machine-learning molecular dynamics simulations”, <https://doi.org/10.5281/zenodo.6671639>.
- [65] <https://github.com/brucefan1983/GPUMD>.
- [66] <https://gpumd.org>.